J. Fluid Mech. (1993), *vol.* 255, *pp.* 447–472

The influence of vortical structures on the thermal fields of jets

By M. D. FOX, M. KUROSAKA, L. HEDGES† AND K. HIRANO‡
Department of Aeronautics and Astronautics, University of Washington, Seattle, WA 98195, USA

(Received 27 December 1991 and in revised form 2 April 1993)

In this investigation we explore the effect of unsteady vortical structures on the adiabatic wall temperature distribution in an impinging jet. Treating first the simpler case of a free jet, we introduce a conceptual model for the separation of the total temperature, appealing to the dynamics of particle pathlines and vortex rings in the jet. The presence of a region of higher total temperature on the inside of the jet and a region of lower total temperature toward the jet periphery, predicted by the model, exhibits good agreement with the experimental data taken at high subsonic Mach number. The results from a numerical simulation further confirm the theoretical expectations.

Through a similar argument, we show that when a thermally insulated flat plate is inserted into the jet, the wall temperature distribution is modified by the presence of secondary vortical structures, which are induced near, and swept over, the plate surface. When the plate is near the jet nozzle, a region of lower wall temperature, attributable to these additional vortices, is observed in the experimental data. When the plate is further from the nozzle, no secondary vortices are formed and no region of lowered wall temperature is measured. Self-sustaining acoustic resonance, when it occurs, is found to alter significantly this picture of the wall temperature distribution.

Although the scope of this work is limited to free and impinging jets, this present topic, along with the previously reported mechanism of the Eckert–Weise effect, exemplifies the wider family of problems in which unsteady vortical structure strongly affects the wall temperature and heat transfer.

1. Introduction

Recent investigations have placed much emphasis on the role of large-scale structures in turbulent flow. However, the fact that vortical structures swept near a body can control its surface temperature – by altering the total temperature distribution in the surrounding fluid – has not in the past received adequate attention.

This idea, which has been explored previously for a wake flow behind a cylinder (Kurosaka *et al.* 1987; Ng, Chakroun & Kurosaka 1990), is pursued here in the context of subsonic free and impinging jets. For the simpler case of the free jet, we will show that the large-scale structures, or vortex rings, formed at the jet periphery determine the total temperature distribution. For the impinging jet, however, it is the *competition* between these vortex rings and secondary vortices induced by them on the impingement plate that determines the nearby total and wall surface temperature distribution. But before proceeding to this topic some general discussion is in order.

† Present address: Boeing Commercial Airplane Company, Seattle, Washington, USA.
‡ Present address: Miyazaki University, Miyazaki, Japan.

Kurosaka *et al.* pointed out that unsteady vortices convected in flows can, in general, separate the total temperature around them into regions of higher and lower total temperature. By applying this concept to a Kármán vortex street it was possible to explain the presence of negative recovery factors on the rear side of a thermally insulated body, known as the Eckert–Weise effect. In this explanation there are two prevailing themes: (i) the global total-temperature separation induced by vortices, and (ii) the effect of this separation on the local wall temperature on the body. These themes manifest themselves again in the present work, and so we discuss them in turn next.

Vortex-induced total temperature separation is essentially an unsteady, inviscid process which can be described by the adiabatic energy equation for a perfect gas,

$$c_p \frac{\mathrm{D}T_t}{\mathrm{D}t} = \frac{1}{\rho}\frac{\partial p}{\partial t}, \tag{1}$$

where T_t is the total temperature. This equation states that the change in the total temperature of a fluid particle along its trajectory is determined by the *temporal* variation of the static pressure, which in a vortex-dominated flow changes its sign depending on the movement of the low-pressure cores of vortical structures relative to the fluid particle. Thus, if the particle sees the approach of a vortex, with its low-pressure core, $\partial p/\partial t < 0$ and T_t decreases along the particle trajectory. If the vortex core is seen to be retreating, however, $\partial p/\partial t > 0$ and T_t increases along the particle trajectory. This variation of the total temperature along particle pathlines is responsible for the presence of hot and cold spots around vortices. In other words, even when the upstream total temperature distribution is uniform, its subsequent distribution around vortices becomes asymmetric (i.e. higher on one side and lower on the other); this is our first theme.

Although Kurosaka *et al.* chose a Kármán vortex street to demonstrate this effect, total-temperature separation is not limited to that case; as long as a flow convects vortices, the vortical structure will cause total-temperature separation. In fact, total-temperature separation can be observed even in vortical structure not as strong as the Kármán vortex street. O'Callaghan & Kurosaka (1992) confirmed the total-temperature separation for the following weak vortical structures: (*a*) those found originally by Brown & Roshko (1974) in a two-dimensional shear layer behind a splitter plate, and (*b*) those occurring downstream of a backward-facing step. The vortices in the latter case are only dimly observable even in flow-visualization studies (e.g. Pronchick & Kline 1983). One might then expect to find total-temperature separation in turbulent jet flows, the subject of this paper, although the vortical structure in an unexcited jet is weaker than that of the Kármán vortex street. Note that the fact that even weak vortical structures leave their imprint in the total-temperature distribution can be exploited in reverse: the presence of such weak structures can be identified by a point-measurement of the total temperature.

Turning now to our second theme, when a stationary body with thermally insulated walls is immersed in a vortical flow, its surface temperature should be regarded as the boundary value of the total temperature, whose distribution is governed by inviscid, unsteady vortex dynamics. Although this interpretation of the wall temperature is not customary, it is nevertheless correct since on the wall, where the flow velocity is equal to zero, the total temperature is equal to the wall temperature. Physically, even the effects of viscosity and thermal conductivity near the wall do not appreciably affect the interpretation, and the reason is as follows.

Consider first a boundary layer over a flat wall, perturbed slightly by an approaching vortex, which is generated elsewhere (for instance, vortices generated behind the

aforementioned splitter plate placed in the middle of a wind tunnel, which approach the tunnel wall downstream). The perturbation is such that it does not induce separation on the wall itself and thus the boundary-layer approximation remains valid. When the wall is thermally insulated, one can show (see the Appendix) that for flows with a Prandtl number (Pr) of unity, the total temperature within the boundary layer does not vary along a vertical line passing through the vortex centre. In other words, the total temperature beneath the vortex core, including the wall temperature, responds without any time lag to the corresponding time-varying T_t outside the boundary layer, the latter being induced by the inviscid vortex dynamics. This is an unsteady generalization of the well-known invariance of the total temperature in steady viscous, parallel flow with $Pr = 1$. Even in unsteady vortical flows, the effects of frictional heating and thermal diffusion mutually cancel, exactly for $Pr = 1$ and substantially for air with $Pr = 0.71$. This enables the vortices in the air stream to impress their total temperature field, almost without attenuation, upon a nearby wall.

Next consider the less tractable case of a vortex separating from the wall itself (e.g. nascent stage of the Kármán vortex). Vortical motion entrains ambient fluid and brings it closer to the wall. This creates a new, instantaneous layered structure localized between the vortex and the wall: an inviscid region consisting of engulfed 'virgin' fluid and a thinner viscous layer on the wall. This situation, then, is not unlike that discussed above, and the same conclusion about total temperature would be applicable.

In the conventional, steady view, unless there is heat or work interaction between the flow and the external environment or the flow is at high speeds, the total temperature is not usually given a prominent role, being passively determined by the static temperature distribution and the velocity profile. On the contrary, for unsteady, vortical flows, we are emphasizing the need to give more attention to the total temperature: the total temperature, whose global distribution is determined by an inviscid mechanism, should be given an active role in interpreting the wall temperature distribution. The usefulness of the total temperature in this sense applies even in the absence of heat or work interaction and even in subsonic flows. In fact, only through an explicit recognition of this role can one arrive at an adequate explanation of the Eckert–Weise effect (Kurosaka *et al.*). This is also the case for the subject of jet flows, to which we now turn our attention and apply the above general discussion.

Recently Goldstein, Behbahani & Heppelmann (1986) measured, for an impinging air jet, the recovery factor (R_f) on the impingement plate surface. The plate was made of thermally insulating material and the measurements were taken with embedded thermocouples. The data showed that R_f plotted against the radial distance from the jet centreline (r) is strongly dependent on the spacing between the jet nozzle and the impingement plate. When the plate is close to the nozzle, R_f at the centreline ($r = 0$) is predictably unity and so are its values for large r. However, within an annular region near the jet centre, R_f decreases sharply to values of less than 0.8. When the plate is further away, R_f at the centreline exceeds unity, another puzzling feature, and it monotonically decreases to unity for large r, without displaying any intermediate decrease to below a value of one.

As will be seen shortly, this interesting result can be explained most conveniently by appealing to the concept of vortex-induced total-temperature separation, an interpretation different from that offered by Goldstein *et al.* To put the impinging jet results in proper perspective, however, we consider first the total-temperature separation in a free jet, and then build on that to investigate the impinging jet. The conceptual models of §§2 and 3 are supported by experimental data, to be presented in §4, and by numerical simulations.

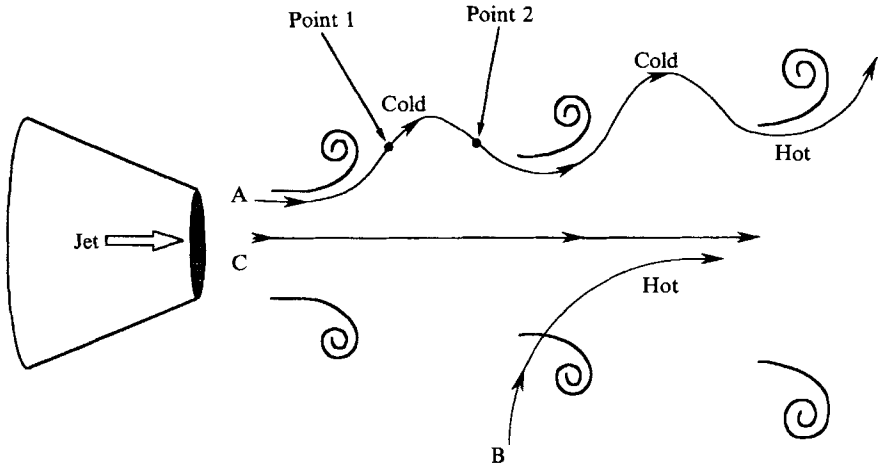

FIGURE 1. Pathlines in a free jet.

2. Total-temperature separation model for the free jet

It is now well established that large-scale structures, or vortex rings, exist at the periphery of a free jet, even at high Reynolds numbers (e.g. Crow & Champagne 1971; Lau & Fisher 1975; Yule 1978; Tso, Kovasznay & Hussain 1981; Dimotakis, Miake-Lye & Papantoniou 1983). It has also been discovered that the strength of these vortical structures, though weak, can be intensified by external excitations (e.g. Zaman & Hussain 1980; Ahuja, Lepikovsky & Burrin 1982; & Badri-Narayan & Platzer 1988). Since the sense of rotation of these vortex rings is opposite to that of the Kármán vortex street, the pattern of T_t separation in the free jet is expected to be, generally speaking, opposite to that of the wake (Eckert 1984, 1986, 1987). The details are, however, subtly different. We discuss this below by considering the pathlines taken by fluid particles, as mentioned in §1. The results from a numerical simulation provide additional support for the pathline argument.

2.1. *Dynamical model*

It is convenient to categorize the fluid particles in jets into three groups: A, particles entrapped by the vortex rings, which rotate around the vortex rings and are simultaneously convected downstream; B, those entrained from the ambient air outside of the jet; and C, those initially discharged near the nozzle centre and which remain near the jet centreline.

Keeping this in mind, consider first the pathline of a particle, belonging to class A, which begins inside the jet. When the particle following this path, labelled A in figure 1, nears the outside of the jet (point 1), at this spatially fixed position the approach of the upstream vortex core with its low-pressure centre results in $\partial p/\partial t < 0$, and T_t falls according to (1). As the trajectory turns back toward the centre of the jet (point 2), the particle sees the vortex moving downstream, with $\partial p/\partial t > 0$, and T_t increases. Thus the T_t of a particle along pathline A reaches a minimum near the edge of the jet and a maximum inside the jet.

A particle belonging to class B will follow a different pathline, labelled B in figure 1. Owing to the rotational sense of the vortex rings, the particle enters the jet as the vortex ring is moving downstream, away from the particle, and $\partial p/\partial t > 0$. Thus any particle which is entrained undergoes an increase in T_t, reaching a maximum value near the centreline of the jet. A class C particle, which is situated near the jet centreline, is

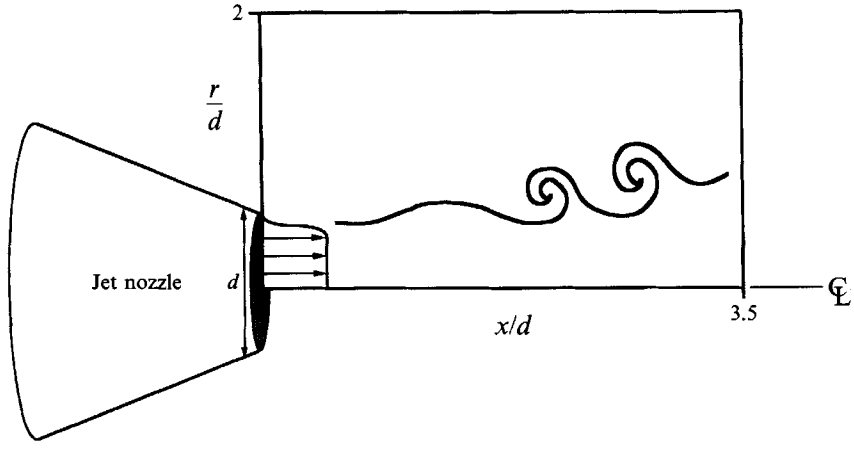

FIGURE 2. Sketch of the computational domain.

virtually unaffected by the vortex rings. Thus its T_t remains essentially unchanged from its far upstream (initial) value.

Near the nozzle, where the entrainment is minimal, the time-averaged radial profile of T_t is expected to show the features of (i) an excess and deficit in T_t near the jet periphery due to particles of class A, and (ii) a region of constant T_t near the jet centreline corresponding to class C particles. As we move further downstream from the nozzle, the entrainment increases, and the higher T_t of the entrained particles, B, will raise the T_t of the jet centre by mixing with particles of class C. Far downstream, then, the jet will possess a higher T_t near the centreline, surrounded of course by an annular region of lower T_t in order to satisfy the heat-flux balance.

2.2. *Numerical simulation of a free jet*

Our conclusions, based on this conceptual model, may most conveniently be confirmed and displayed with the aid of numerical simulation. The computational model adopted here is a compressible axisymmetric jet, whose computational domain is sketched in figure 2. For simplicity, the fluid is treated as an inviscid, non-heat-conducting gas. In this simulation the unsteady Euler equations are solved with Harten & Yee's (1985) total variation diminishing finite-difference technique. This scheme provides, if needed, a non-oscillatory shock-capturing ability with minimal diffusion and gives the physically consistent solution satisfying the entropy condition. The scheme does not add dissipation where the flow is smooth and no damping is required, but can add large amounts of dissipation at shock points or regions of steep gradients where damping is required.

Runge–Kutta time advancement is implemented for second-order accuracy in time. In addition, a very small time step is chosen and is fixed for all iterations. A nominal Courant number of between 0.1 and 0.3 was chosen for all simulations; however, the actual Courant number over most of the flow was considerably smaller.

The mean flow is initialized with uniform static pressure and uniform total temperature to approximate the experimental conditions described later. At the inflow a hyperbolic tangent velocity profile in the axial velocity u is imposed, and a broadband white noise perturbation is added to the radial velocity v as a function of time. The perturbation is given by

$$v' = \epsilon G(y) \sum_{j=1}^{j_{max}} \cos(\omega_j t + \phi_j), \tag{2}$$

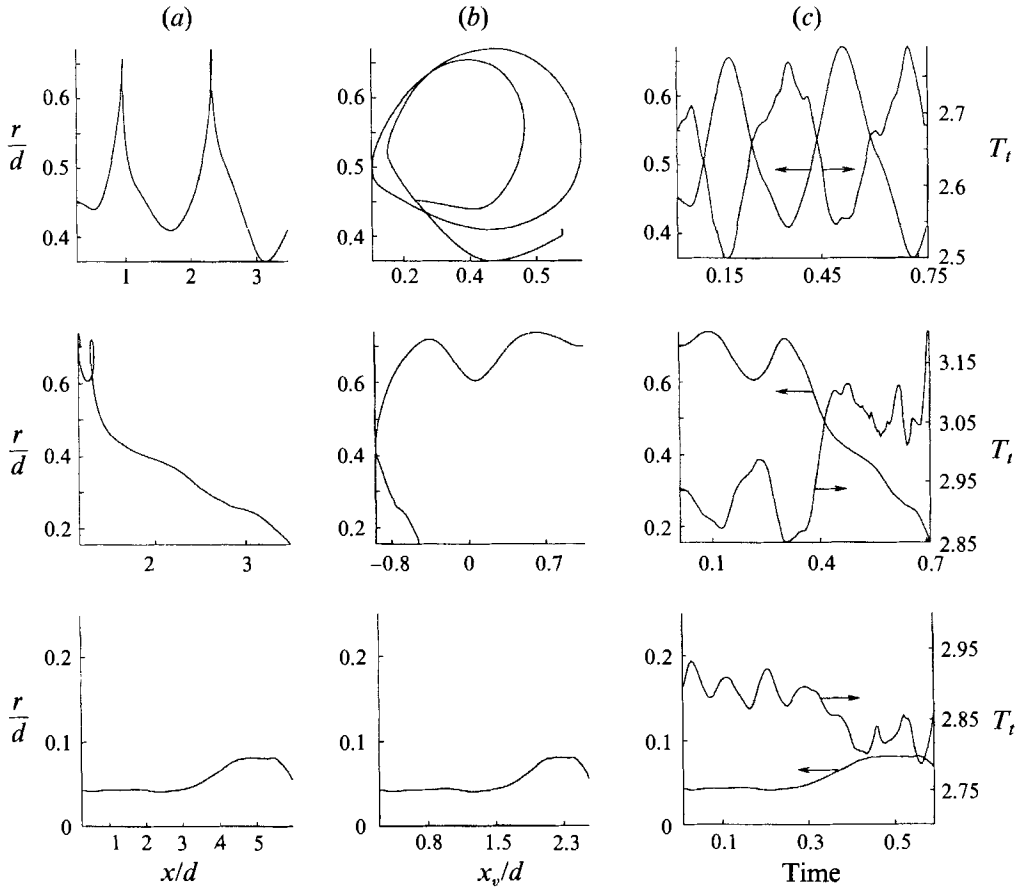

FIGURE 3. Computed particle pathlines and total temperature for a type A pathline (top); a type B pathline (middle); and a type C pathline (bottom). (*a*) Laboratory coordinate frame, x, (*b*) coordinate frame attached to the vortices, x_v, (*c*) total-temperature variation together with corresponding pathline.

where $G(y)$ is a Gaussian forcing function and the amplitude of the perturbation is given by ϵ. The applied frequencies ω_j are equally spaced, with the minimum and maximum values chosen using linear stability theory to bracket the unstable range of frequencies. A randomly determined phase angle ϕ_j is selected for each frequency.

A symmetric boundary condition is used at the bottom of the computational domain (the jet centreline), and a non-reflecting outflow boundary condition is used at the top. To enhance the visualization of coherent structures, a passive scalar field is used to simulate a chemical reaction between reactants in the top and bottom streams. For additional details on the computation, see Hedges (1991) and Hedges & Eberhardt (1992). The simulations were performed for Mach numbers $M = 0.3$, 0.6 and 0.9, covering the range of the experiments presented in §4.

Figure 3 shows three particle pathlines from the numerical simulation corresponding to types A, B, and C from the conceptual model. In figure 3(*a*) the pathlines are plotted in the laboratory coordinate frame, x, while figure 3(*b*) show the same pathlines in a coordinate frame, x_v, attached to and travelling at the average speed of the vortices. Figure 3(*c*) shows the total-temperature variation along with the corresponding path-

line for each case, plotted against time. The particle of type A, which is trapped around a vortex, undergoes a cyclic total-temperature fluctuation, becoming cooler toward the jet periphery and warmer toward the jet centreline. The total temperature of the type B particle, entrained from the surrounding ambient air by a passing vortex, increases as the particle enters the jet, and reaches a maximum value at the centreline. Particle C, which always remains near the jet centreline (note that the radial values of the pathline for this type are smaller than for the others) feels little change in total temperature. Although many other pathlines may be plotted, they can all be categorized as possessing one of these three basic behaviours. These particle pathline computations clearly substantiate the model proposed in §2.1.

Figures 4(*a–c*) are instantaneous snapshots of the $M = 0.9$ jet at three different times, showing the vortical structure (as visualized by the chemical reactant concentration), static pressure, and total temperature for each time. Each reveals the expected total temperature separation around the vortices. Even in the very near field, before the structures are barely recognizable as vortices, the total-temperature separation is apparent. Further downstream, the pairing process is observed to enhance the total-temperature separation.

Figure 5 shows, for Mach numbers of 0.35, 0.6, and 0.9, the temporal average of the total-temperature distribution. Here one can clearly see the encroachment of the hot region into the jet centreline with increasing distance from the nozzle. These time-averaged results, which correspond to those taken with a slow-response probe, will be compared later to experimental data obtained with a total-temperature probe; although an exact comparison is not possible because of the absence of an initial boundary layer and the imposed uniformity of the static pressure at the inflow, good agreement in overall features is observed, confirming that the numerical simulations capture the correct physics. (The time-averaged static temperature field shows the expected distribution (thus not included here): initially higher static temperature on the ambient side and lower static temperature within the jet, corresponding to the uniform total temperature initially imposed; this becomes diffuse as the mixing layer grows in the downstream direction.)

3. Impinging jet

When a flat plate is inserted normal to a jet, the total temperature separation in the resulting impinging jet is modified by additional (secondary) vortex rings on the impingement plate, induced by the approach of the vortex rings (primary) formed at the nozzle lip.

As is well known, when a vortex approaches a rigid wall the accompanying unsteady adverse pressure gradient induces a separation of the wall boundary layer, which rolls up into a counter-rotating vortex. Thus it is not unexpected, and in fact has been confirmed, that an isolated vortex ring generated in an otherwise stagnant fluid induces a secondary vortex ring upon impact with a wall (Magarvey & MacLatchy 1964; Schneider 1980; Yamada & Matsui 1980; Walker *et al.* 1987). Although, even in an impinging jet, such a secondary vortex has been observed (Didden & Ho 1985), what has surprised us is the orderliness and extent of the row of secondary vortices in an impinging jet. Figure 6 (plate 1) contains a series of photographs taken by us in a water-jet facility (to be described in §4), showing both the primary and secondary vortices alone, and together†. Primary vortices, formed at the nozzle lip, approach the

† While the manuscript of the present paper was prepared, it came to our attention that recently Popiel & Trass (1991) also obtained photos of secondary vortices in an impinging jet at a higher

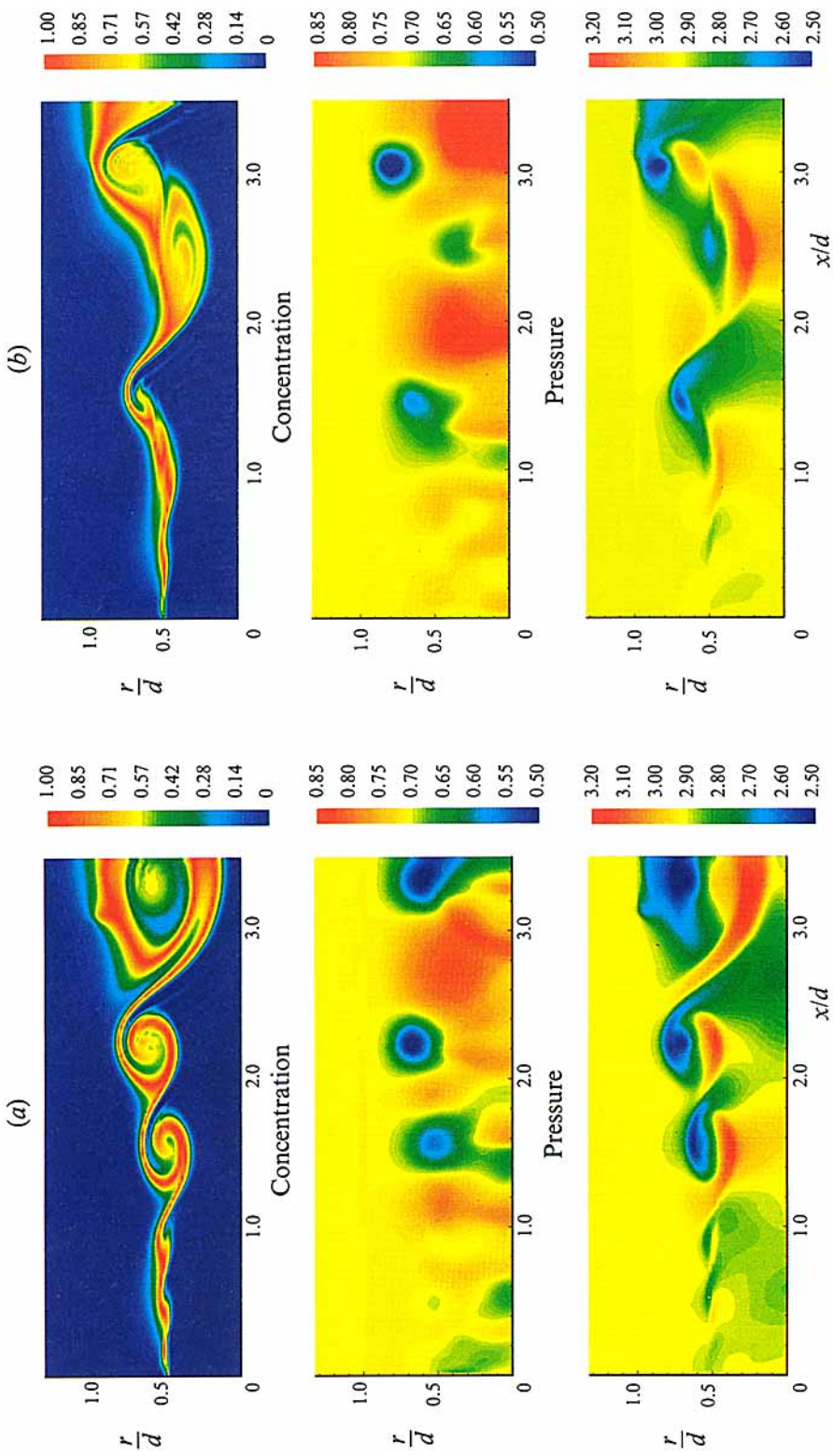

FIGURE 4 (*a*, *b*). For caption see facing page.

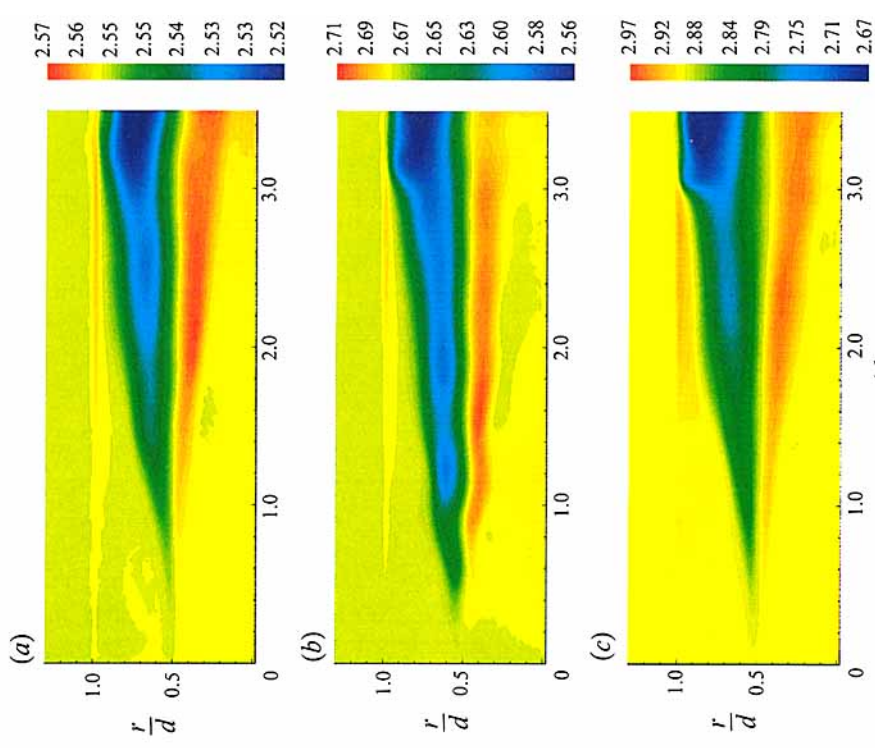

FIGURE 5. Time-averaged total-temperature distribution in a free jet; (*a*) $M_j = 0.35$, (*b*) $M_j = 0.6$, and (*c*) $M_j = 0.9$.

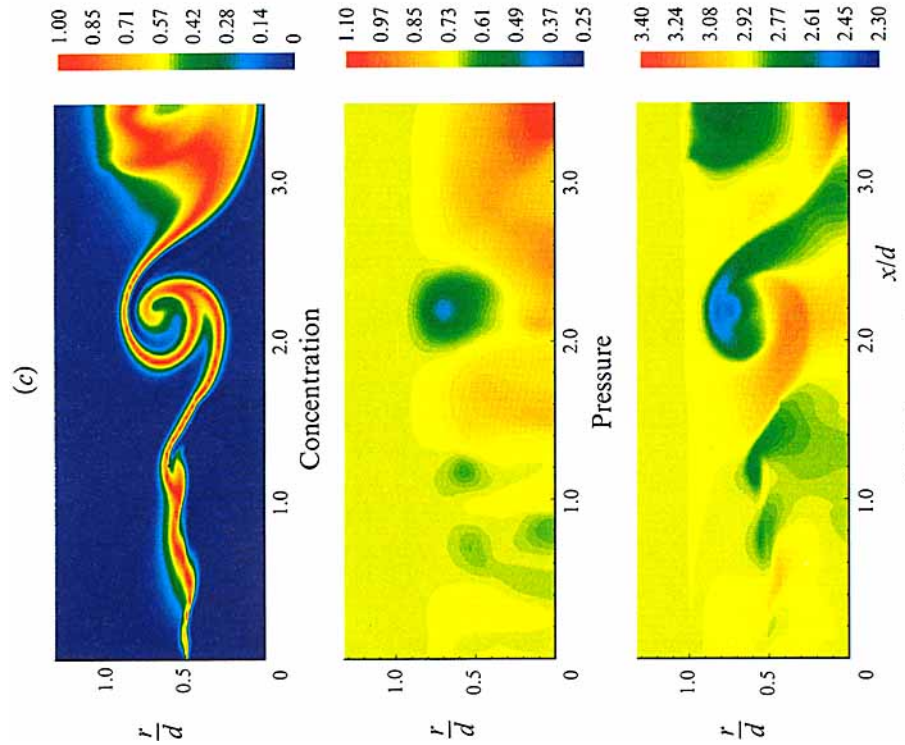

FIGURE 4. Instantaneous snapshot of the $M_j = 0.9$ jet at (*a*) time $t^* = 105$, where t^* is non-dimensionalized by U_j and the nozzle radius; (*b*) $t^* = 108.3$; and (*c*) $t^* = 111.6$.

impingement surface and generate counter-rotating secondary vortices; the latter move radially outward along the plate surface, in phase with the former. In other words, each of the secondary vortices formed in a row is precisely locked to, and moves with, the corresponding primary vortices.

The presence of secondary vortices, however, depends on the separation distance between the impingement plate and the nozzle. When the ratio of nozzle–impingement plate spacing (x) to nozzle diameter (d) is small, the primary vortex rings approach the surface near the stagnation point, where the momentum of the wall boundary layer is low. The unsteady adverse pressure gradients will overwhelm the low momentum, and cause the boundary layer to separate and roll up into secondary vortex rings. At large x/d, however, the primary vortex rings approach the plate at a larger radial distance from the stagnation point. The boundary-layer momentum is greater and no separation occurs.

Thus the presence of secondary vortex rings is determined by the competition between two factors: (i) the adverse pressure gradient around the primary vortex rings, given by $\partial p/\partial r_c$ (where r_c is the radial distance from the centre of the primary vortex ring), and (ii) the gradient of the momentum in the wall boundary layer, given by $\rho u_r \partial u_r/\partial r$ (where u_r is the radial velocity within the boundary layer and r is the radial distance from the jet centreline). A simple consideration of the ratio between these factors (near the stagnation point) leads to the conclusion that the criterion for existence of the secondary vortex rings depends on x/d, and is independent of the Mach number and the Reynolds number for the subsonic cases presented here. The water jet experiments have shown that for values of x/d beyond 6, secondary vortex rings are no longer formed.

The same dynamical argument that was applied to the total-temperature separation in a free jet can now be used to explain the behaviour of the total temperature around the secondary vortex rings when they exist, for small x/d. Imagine a particle that is originally entrained from outside the wall boundary layer, which is convected radially along the plate surface while it rotates around the secondary vortex. Because the rotational sense of the secondary vortex rings is opposite to that of the primary vortex rings, the particle sees a decrease in the static pressure as its trajectory approaches the plate surface; $\partial p/\partial t < 0$ and the total temperature of the particle falls. Thus the cooling appears, as shown in figure 7(a), between the secondary vortex rings and the plate; the heating appears between the secondary and primary vortex rings. The former results in a region of cooling on the plate surface itself, as discussed in the Introduction. For larger x/d, the primary vortex rings exist alone. The situation, then, is similar to the free jet in the far field, but the deflection of the jet by the wall causes only the heating to appear on the plate surface, as shown in figure 7(b), with the point of maximum heating located at the jet centre.

This picture of the total temperature separation has recently been confirmed by another numerical simulation. Mr. Jalamani of NASA Ames Research Center kindly sent us his computational results corresponding to $x/d = 4$, based on an unsteady Navier–Stokes solver (Jalamani, Van Dalsem & Nakamura 1990), which illustrate good agreement with our conceptual model, including the behaviour of the total-temperature separation near the plate surface: cold spots with lower T_t are generated between the wall and the secondary vortices, which act to shield the hot spots with higher T_t that are located between the secondary and primary vortices. Characteristic of this intermediate value of x/d, a region of higher T_t also exists, at and around the

Reynolds number of 20000. It is of interest to note that the general features of the secondary vortices are similar to those of figure 6, corresponding to a lower Reynolds number.

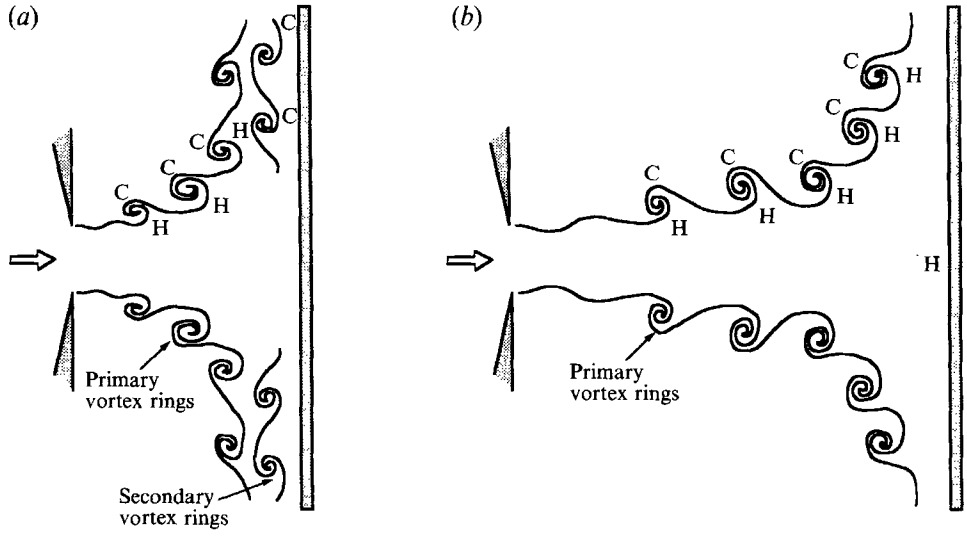

FIGURE 7. Schematic of the instantaneous total-temperature separation in an impinging jet: (*a*) small x/d; (*b*) large x/d. C denotes cold and H hot.

jet centreline. These general features may also be observed in the time-averaged wall temperature data of figure 11.

The question might be raised of whether the vortices observed in a low-Reynolds-number regime might persist even at such high Reynolds numbers as used in the experiments to be described shortly. We feel that this is almost certainly the case based on the following reasoning. The fact that primary vortices exist at a Reynolds number of 2.3×10^6 has now been confirmed for a supersonic jet by Lepicovsky *et al.* (1986). This is not surprising in view of the fact that in a two-dimensional shear flow, large-scale structures are found to persist to Reynolds numbers of 10^7 (Dimotakis & Brown 1976). The criterion for the generation of secondary vortices is, as mentioned, independent of the Reynolds number as well as the Mach number; therefore there is no reason to expect that secondary vortices would not also exist at high Reynolds numbers. It should be emphasized that the proposed mechanism of total-temperature separation in an impinging jet rests only on the presence or absence of the secondary vortices and not on the details of their structure, which may or may not depend on the Reynolds number.

4. Experiments

The air-jet facility constructed for this work is shown in figure 8. Air supplied in blow-down fashion is heated to adjust the incoming air total temperature and maintain it constant during a test. Background noise emanating from the upstream valves and piping is reduced by a foam-lined settling tank, and the nozzle (interchangeable from 0.3175 cm to 10.16 cm diameter) and impingement plate are located in an anechoic test chamber designed to eliminate spurious acoustic reflections. The settling tank is fitted with mounts for four speakers evenly spaced around the circumference, providing the capability to externally force the jet. The speakers are driven by two 120 W audio amplifiers. The far-field frequency spectra in the test chamber are measured by a Brüel and Kjær Type 4136 condenser microphone and Type 2033 high-resolution FFT analyser. The impingement plate surface is made of acrylic, a thermally insulating

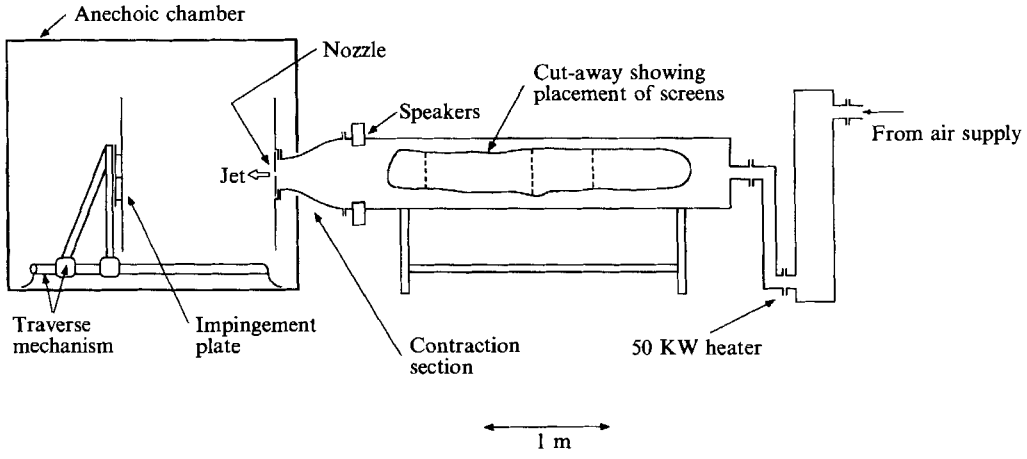

FIGURE 8. Test apparatus.

material, because if a thermally conducting material were to be used, conduction within the plate would interfere with the thermal separation effect produced by the vortex rings. This plate is instrumented with 88 thermocouples and 46 pressure taps, and the distance between plate and nozzle is controlled by a digital stepping motor to an accuracy of 0.05 mm. Temperature and pressure data are recorded by a Fluke 2204A Scanner and a Scanivalve® Model J respectively. Both the data collection and the stepping motor are controlled by an IBM PC-AT (a Macintosh IIci is used for the free jet data collection). Total temperature in the free jet is measured with a United Sensor YCT-156 probe with its open end facing upstream, and 5 and 10 cm diameter nozzles are used for best resolution. Impinging jet tests were conducted with the jet Mach number (M_j) between 0.6 and 0.9, and with x/d ranging from 0.25 to 30.

For all of the impinging-jet data presented in this paper, an orifice-type nozzle with a sharp-edged lip was used. This configuration results in the simplest geometry, with a flat surface at the nozzle exit plane, and a flat impingement plate. For the free-jet work, however, two contoured, convergent-type nozzles were used. These nozzles have diameters of 5 and 10 cm, and the nozzle lips are sharp edges, as before.

The photographs of the free and impinging jets shown in figure 6 (plate 5) were obtained in a water tunnel which was modified from an existing $1.5 \times 1.5 \times 1.5$ m water tank. Two 2.5 cm nozzles fitted with dye taps were used: one was fitted with individual dye injection ports, useful for obtaining a cross-section of the primary vortex ring, and the other had a continuous slot milled around the nozzle lip into which dye was introduced. Dye was released from a single port on the impingement plate to obtain the cross-sections of the secondary vortex rings. Care was taken in all cases to ensure that the dye injection did not interfere with the jet flow, and the specific gravity of the dye was matched to that of the water in the tank to eliminate any buoyancy effects. The Reynolds number of the jet based on its diameter is 400 for the photographs in figure 6 (plate 1).

4.1. *Free-jet results*

Radial profiles of the time-averaged total temperature distribution $\langle T_t \rangle$ in a free jet are plotted in figure 9, for several values of x/d. For these tests $M_j = 0.9$. Here and elsewhere the reservoir total temperature is held constant and equal to the ambient temperature, eliminating any temperature changes due to entrainment of ambient air (in figure 9, as well as in subsequent figures, T_0 refers to the reservoir total temperature).

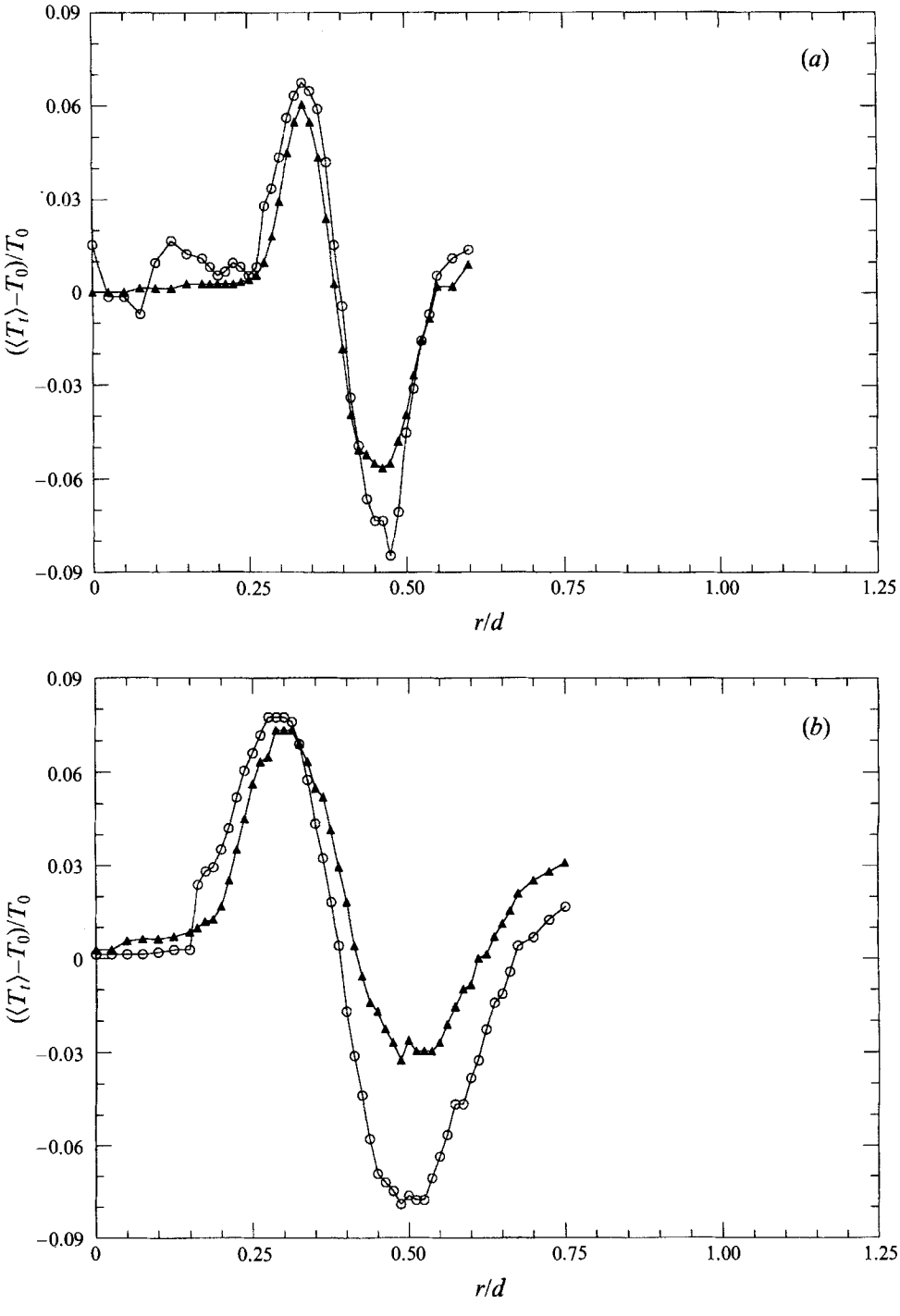

FIGURE 10 (*a*, *b*). For caption see facing page.

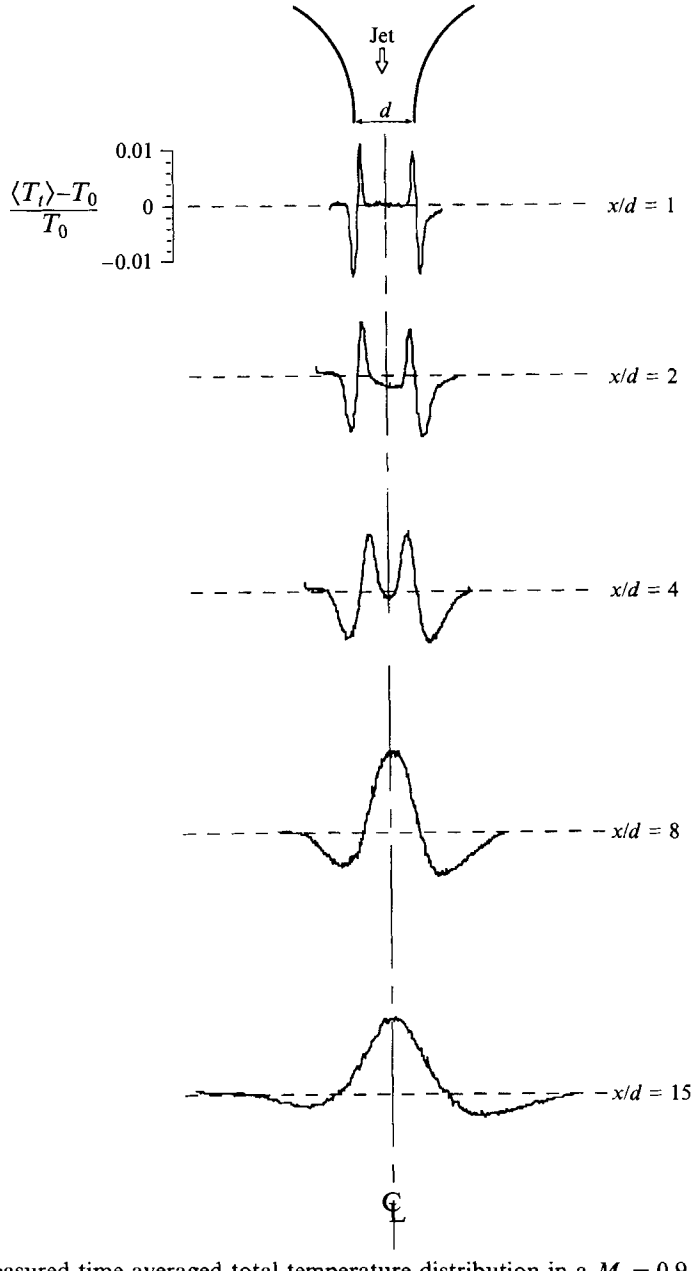

FIGURE 9. Measured time-averaged total-temperature distribution in a $M_j = 0.9$ free jet at various downstream distances; the jet diameter, d, is 5 cm.

The measured $\langle T_t \rangle$ agrees with the physical expectations discussed earlier. The near-field is characterized by a sharp $\langle T_t \rangle$ separation, as much as 5 °C; this becomes spread out as x/d increases and the region of heating progresses toward the centre. In the far field, the heating at the jet centre becomes dominant, and is surrounded by a region of cooling greatly reduced in magnitude. This centreline heating was briefly reported three decades ago by Glassman & John (1958) as an unexplained phenomenon.

The key reason for the agreement between the inviscid prediction and the measurements is entrainment of fluid uncontaminated by viscous effects; not only are

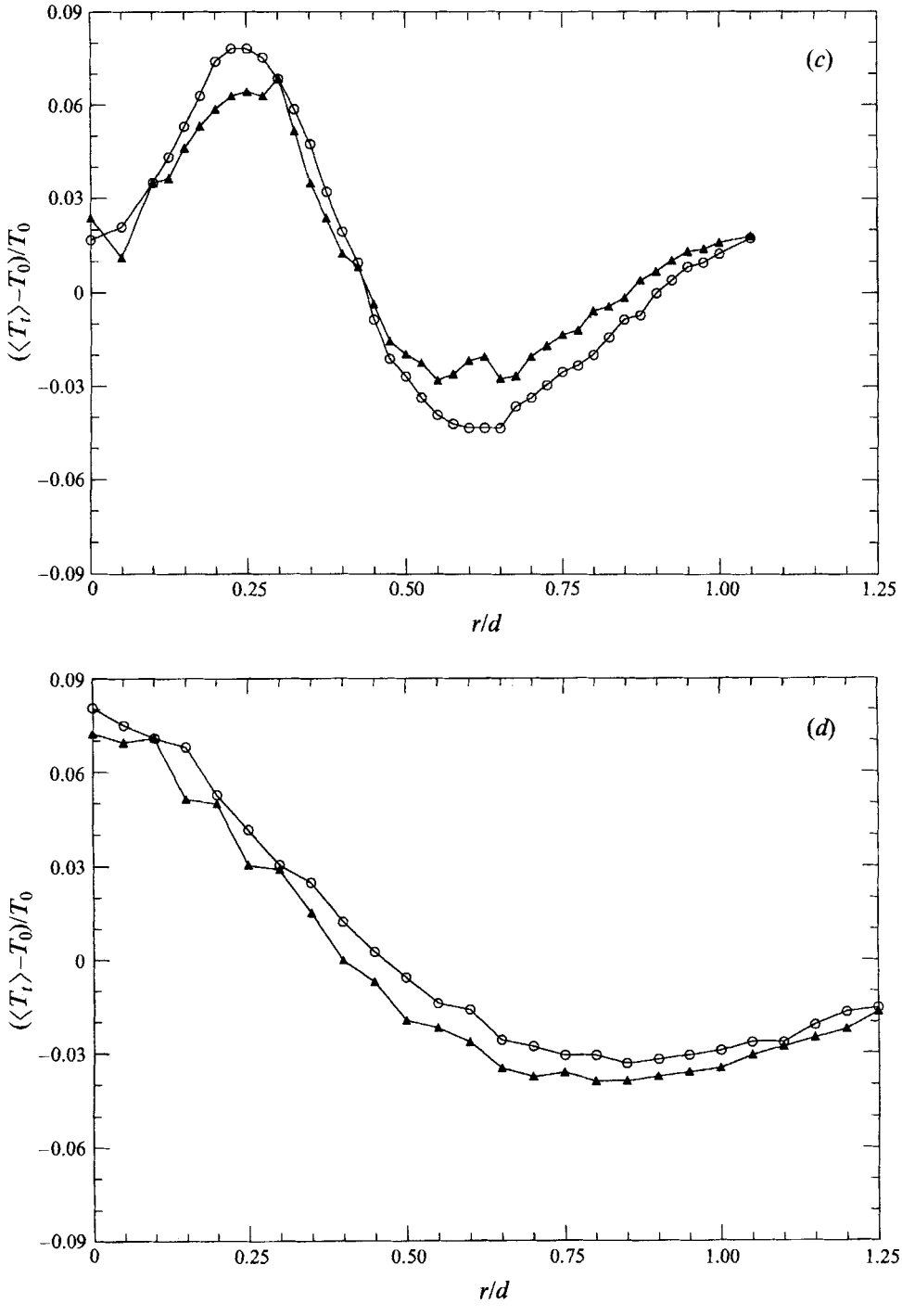

FIGURE 10. Comparison of the measured time-averaged total-temperature distribution in a $M_j = 0.7$ free jet with and without acoustic excitation. Solid triangles are without excitation; circles are with excitation at 2250 Hz. (*a*) $x/d = 1$; (*b*) $x/d = 2$; (*c*) $x/d = 4$; (*d*) $x/d = 8$. The jet diameter, d, is 10 cm.

those fluid particles belonging to class B of §2.1 entrained from the ambient air, but most of the particles belonging to class A, which are trapped around the vortex rings, are also entrained initially from the uncontaminated flow outside of the nozzle boundary layer.

The trends observed in the numerical simulations of the total temperature distribution in a free jet compare favourably with the experimental results. The magnitude of the time-averaged T_t separation in both cases increases by roughly the same proportion as the Mach number is raised from $M_j = 0.35$ to $M_j = 0.6$ and again to $M_j = 0.9$. In both the experiments and the computations, the peak magnitude of the cooling is seen to be greater than the peak magnitude of the heating in the near field. This may be attributable to the longer residence time of fluid particles in the cooling cycle, where the flow speed is low on the ambient side of the jet. Finally, the encroachment of the region of higher $\langle T_t \rangle$ toward the centreline, due to the dominant influence of entrainment in the far field, is observed in both the experiments and the simulations.

Since acoustic excitation can intensify the vortical structure, which should in turn increase the total-temperature separation, the jet was excited acoustically and its total temperature was measured. The excitation was applied by four speakers mounted on the settling tank, just upstream of the nozzle. The speaker frequency, 2250 Hz, was matched to the primary longitudinal mode of the settling tank in order to obtain a high-amplitude signal at the nozzle exit plane, and the jet velocity and nozzle diameter were adjusted so that the speaker frequency was close to the first harmonic of the natural jet vortex-shedding frequency. Figure 10 shows a direct comparison between the radial profiles of $\langle T_t \rangle$ for the unexcited jet and the excited jet. For all x/d locations an increase in the magnitude of the $\langle T_t \rangle$ separation is observed.

4.2. *Impinging-jet results*

Typical radial distributions of the time-averaged wall temperature $\langle T_w \rangle$ and time-averaged wall pressure $\langle p_w \rangle$ are shown side by side in figure 11 (here $\langle p_w \rangle$ is the absolute static pressure, and p_a is the absolute atmospheric pressure). Note that while, as mentioned, the reservoir total temperature T_0 is matched to the ambient temperature, the reservoir total pressure is of course higher than the ambient pressure p_a; the latter appears as a pressure peak at the stagnation point.

The gross features of the $\langle T_w \rangle$ distributions are again in essential agreement with those derived from the conceptual model, which are described in §3 and shown schematically in figures 7(*a*, *b*): cooling at small values of x/d and heating at larger values of x/d. The plotted magnitude of the cooling in the near field corresponds to a measured wall temperature more than 12 °C below the ambient temperature of 20 °C. The secondary vortex rings are relatively closer to the plate surface than the primary vortex rings and, as discussed, it is the influence of the former that is felt on the wall. In other words, the cooling induced by the secondary vortex rings serves to thermally shield the plate by forming a cold 'blanket', which extends several nozzle diameters along the plate. It is interesting to note that the radial extent of the secondary vortex rings observed in the flow visualization, figure 6 (plate 1), is also in the same range, despite the vast differences in the Reynolds numbers. (Although in the near field only cooling is observed, the heat flux balance is of course satisfied since at large radial distances from the stagnation point the wall temperature is the same as the initial total temperature of the jet.)

A notable feature of the $\langle p_w \rangle$ distribution is the presence of suction on the impingement surface at small values of x/d. The radial position of the suction, at

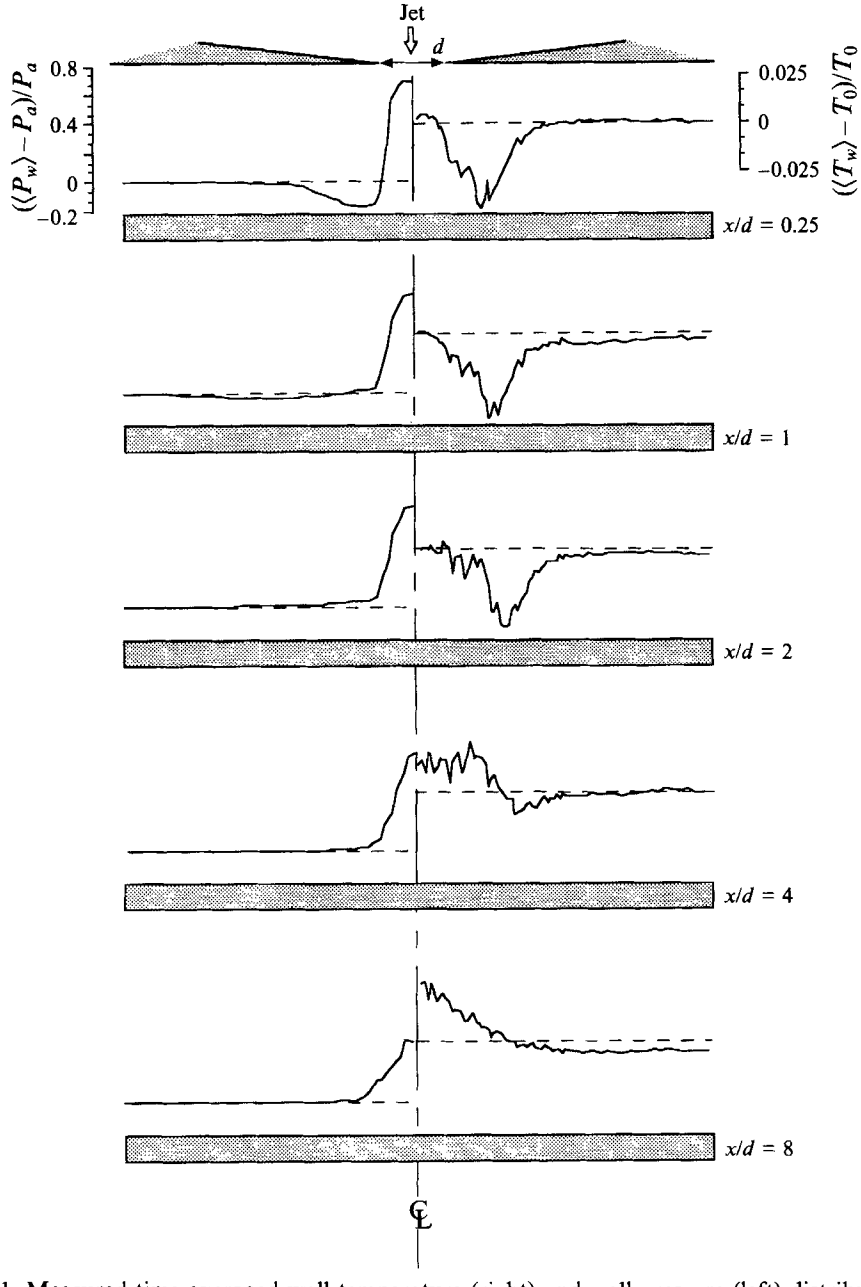

FIGURE 11. Measured time-averaged wall temperature (right) and wall pressure (left) distributions in a $M_j = 0.9$ impinging jet at various downstream distances; d is 5 cm.

$x/d = 0.25$ for instance, roughly corresponds to that of the minimum $\langle T_w \rangle$, and it is interpreted to represent a 'footprint' of the low-pressure cores of the secondary vortex rings.

In the far field, the loss of cooling is consistent with the previously noted disappearance of secondary vortex rings for larger values of x/d (see figure 7*b*); the dominant presence of heating around the jet centreline is, as for the free jet, due to the entrainment of class B fluid particles previously discussed. These $\langle T_w \rangle$ data have the

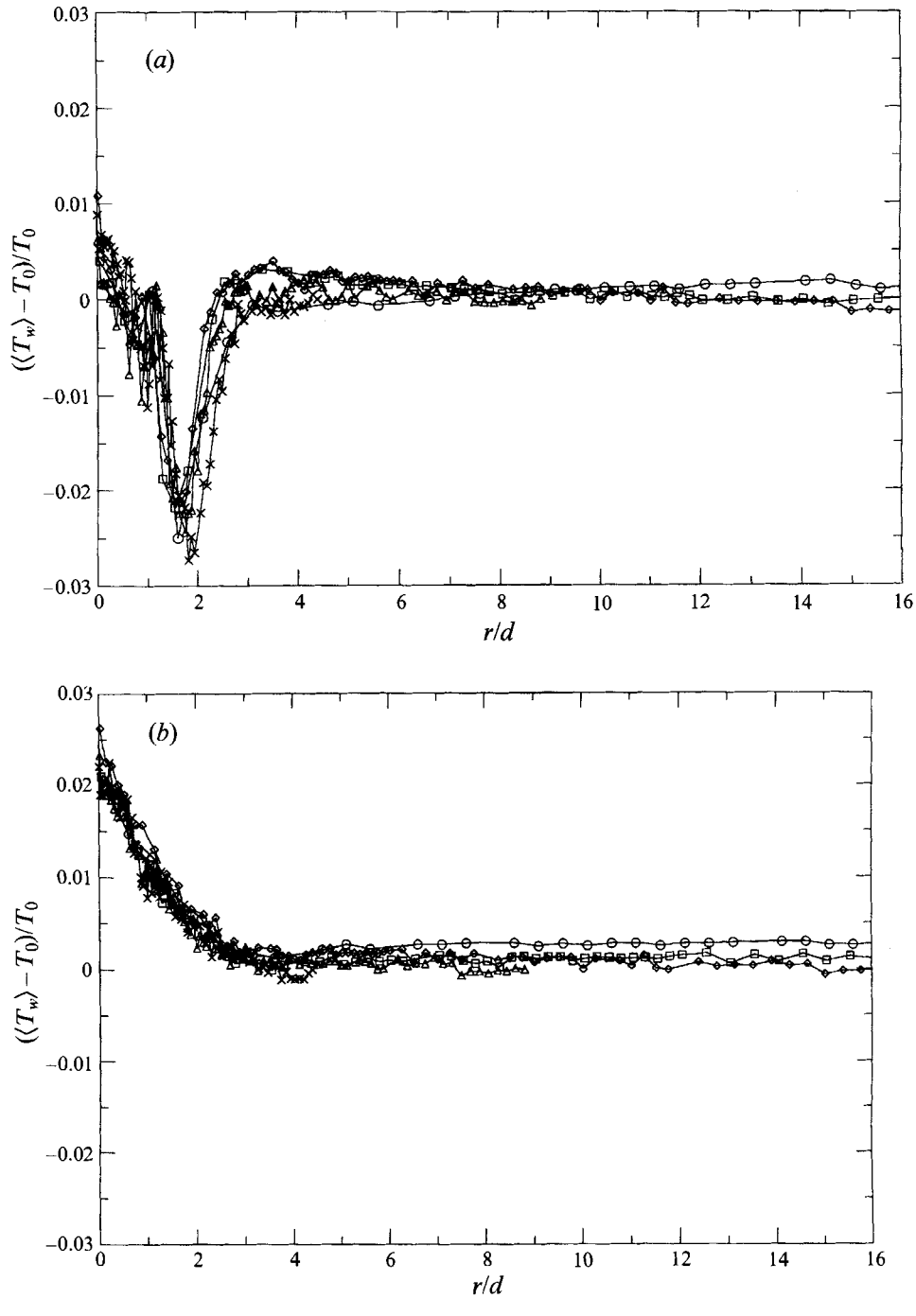

FIGURE 12. Correlation of the measured time-averaged wall temperature distribution with nozzle diameter; (*a*) $x/d = 2$, (*b*) $x/d = 8$, and $M_j = 0.8$. ○, $d = 0.635$ cm; □, $d = 1.27$ cm; ◇, $d = 2.54$ cm; △, $d = 5.08$ cm; ×, $d = 10.16$ cm.

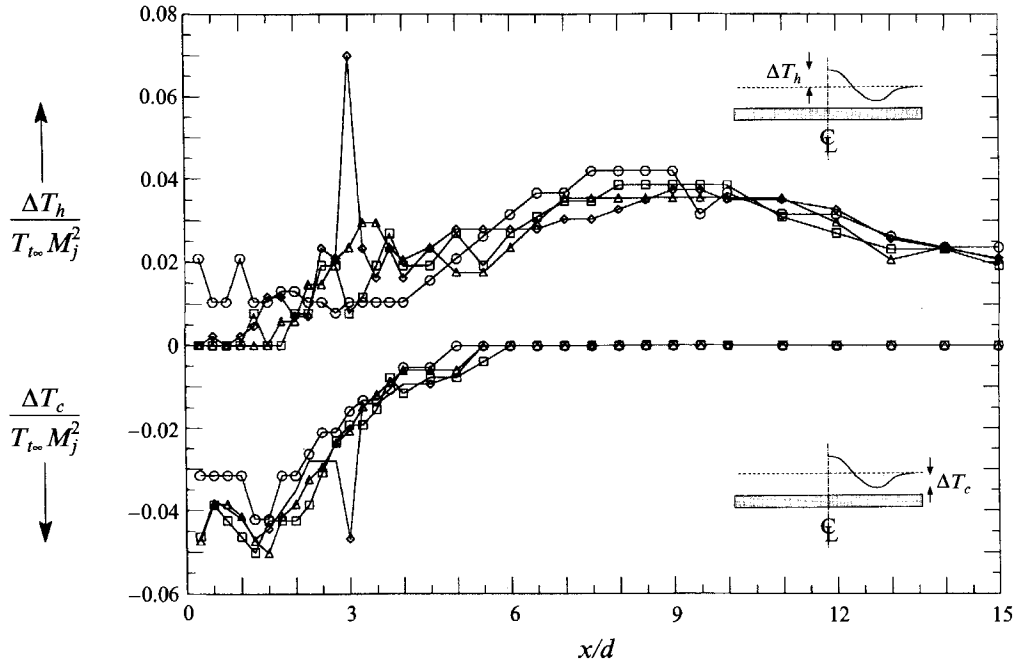

FIGURE 13. Correlation of the maximum heating ΔT_h and cooling ΔT_c with x/d, for several Mach numbers. ○, $M_j = 0.6$; □, $M_j = 0.7$; △, $M_j = 0.8$; ◇, $M_j = 0.9$.

same general features as those obtained by Goldstein *et al.* for a low Mach-number range of 0.2 to 0.4.

The radial profiles of the wall temperature are independent of the nozzle size, when the radial distance, r, is normalized by the nozzle diameter. This is demonstrated by figures 12(*a*, *b*). In each figure we plot the normalized wall temperature versus r/d, for nozzle diameters ranging from 0.635 to 10.16 cm; this corresponds to a Reynolds-number range of 113000 to 1800000 for the present $M_j = 0.8$. Figure 12(*a*) is in the near field, at $x/d = 2$; figure 12(*b*) is in the far field, at $x/d = 8$. In both cases the data are shown to be independent of the nozzle diameter, as well as Reynolds number.

Figure 13 displays the maximum amount of heating and cooling in the radial profile of $\langle T_w \rangle$, plotted with Mach number as a parameter. In the near field ($x/d < 2$), there is significant cooling and little heating, as mentioned. In the far field ($x/d > 4$), $\langle T_w \rangle$ increases to a maximum value around $x/d = 9$ and then drops as the jet diffuses. In both regions the maximum wall temperature separation is a strong function of Mach number, as expected. (The criterion, discussed in §3 and shown to be independent of the Mach number as well as the Reynolds number, applies only to the *existence* of the secondary vortices and obviously not to the magnitude of the T_t separation.)

4.3. *Effect of acoustic resonance*

In figure 13, spiky peaks of heating and cooling are observable for $M_j = 0.9$, in the intermediate region of $x/d = 3$. At this seemingly anomalous point a loud sound is heard; the corresponding pure tones are shown in figure 14(*a*), which displays the frequency spectrum received by a microphone in the far field. The radial profile of $\langle T_w \rangle$ showing the peaks of both heating and cooling is plotted in figure 14(*b*). Figure 14(*c*) shows the corresponding sound-intensity distribution of the fundamental, measured by traversing the microphone in the x-direction while holding its radial position constant.

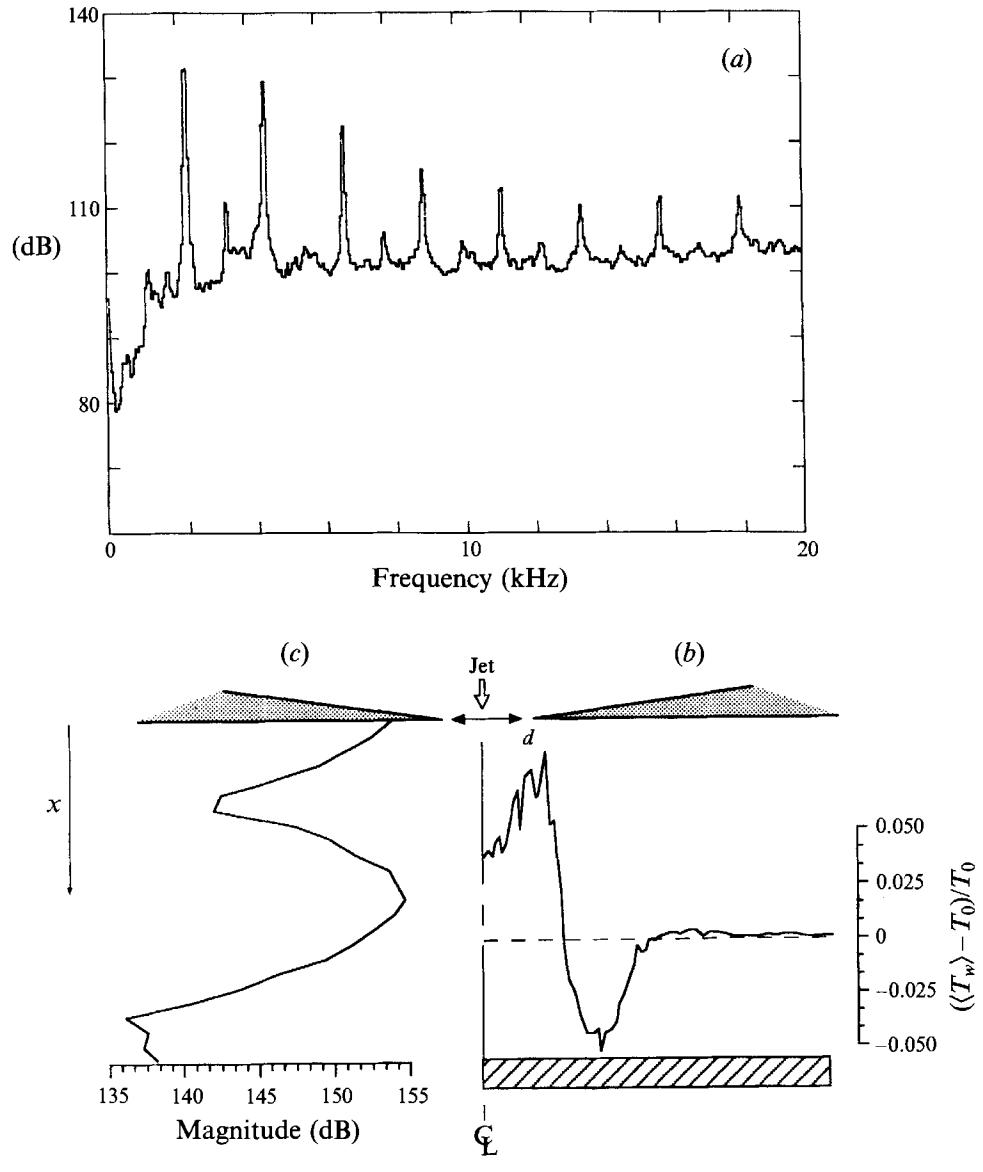

FIGURE 14. Results for the $M_j = 0.9$ impinging jet at $x/d = 3$; (*a*) far-field frequency spectrum for the bare metal nozzle; (*b*) wall temperature distribution at resonance; (*c*) sound intensity distribution of the primary resonant frequency at various x-locations. d is 5 cm.

This intensity distribution essentially corresponds to the second mode of a one-dimensional standing wave, although the presence of a wall jet somewhat depresses and obscures the tonal sounds near the impingement plate. This latter is known as the 'haystack' effect (e.g. Cumpsty 1978), which results from the refraction of the acoustic signal by turbulent motions within the wall jet; the frequency spectrum of the transmitted signal there shows the characteristic frequency broadening.

Thus the present acoustic resonance appears to involve more than the usual phase-lock mechanism proposed by Ho & Nossier (1981). They found that a feedback loop is created by the downstream convection of the vortex rings and the upstream travel

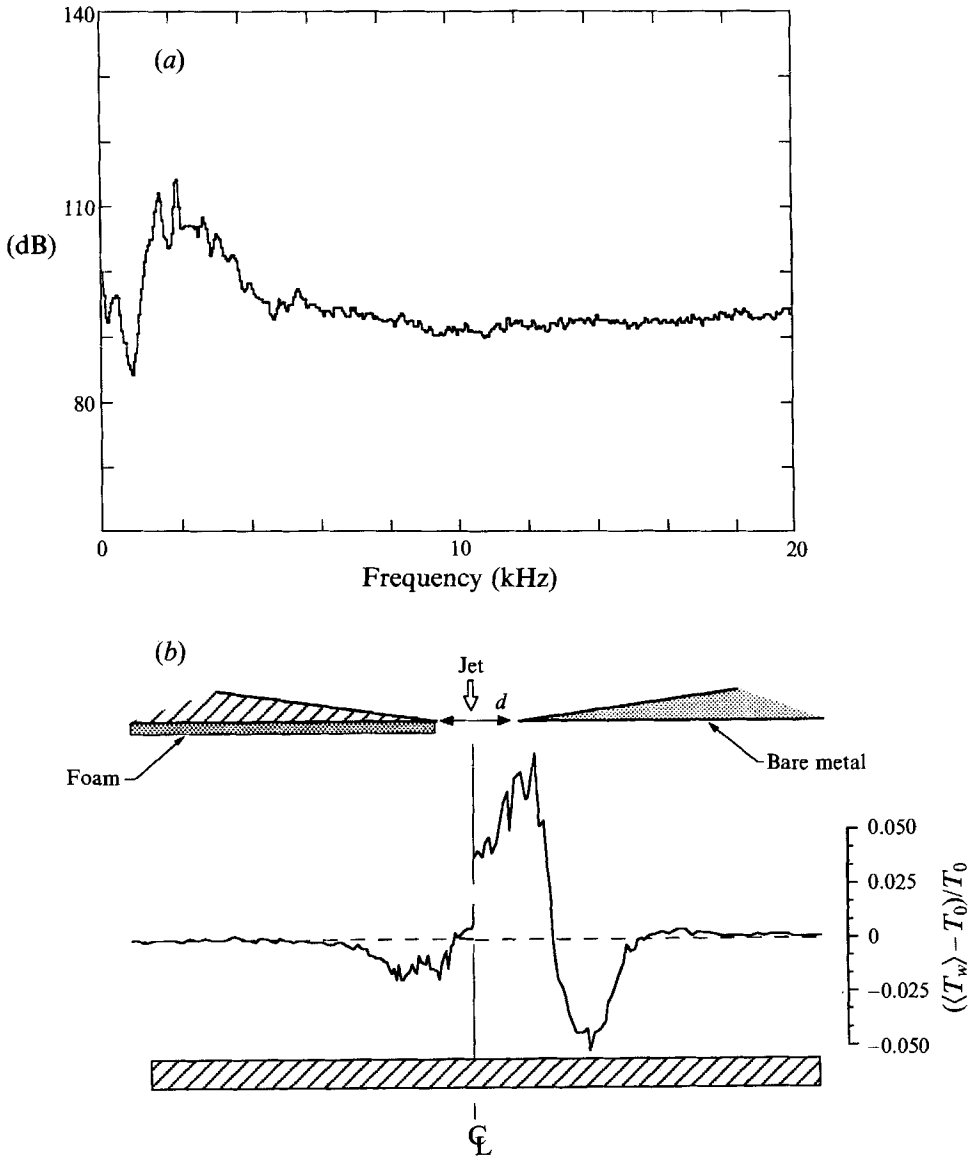

FIGURE 15. Comparison of the results for the $M_j = 0.9$ impinging jet with and without acoustic absorbing foam surrounding the nozzle; (*a*) far-field frequency spectrum for the acoustically treated nozzle; (*b*) side-by-side comparison of the wall temperature distribution with (left) and without (right) the foam.

of acoustic waves formed as the vortex rings impinge on the plate. Allowing only integer multiples of events, the following equation expresses the phase-lock constraint:

$$\frac{x}{a}+\frac{x}{u_v}=\frac{n}{f_v}, \tag{3}$$

where a is the acoustic speed in the ambient air, u_v is the convective speed of the vortical structure (about 60% of the jet speed according to Wagner 1971), f_v is the vortex shedding frequency, and n is an integer; acoustic refraction by the wall jet is ignored.

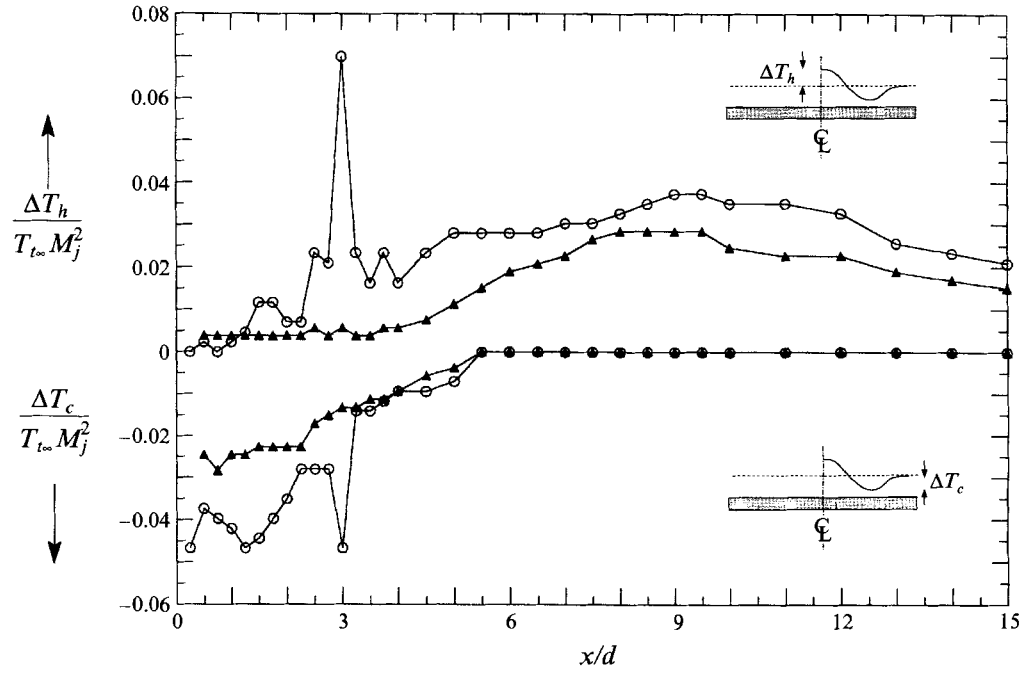

FIGURE 16. Comparison of the maximum ΔT_h and ΔT_c at different x/d locations for the bare metal nozzle (○) and the acoustically treated nozzle (▲); the jet Mach number is 0.9.

In addition to the above phase-lock mechanism, however, in our experiments the geometry of the test rig is such that a standing wave can be formed in the ambient air between the impingement plate and the flat wall surrounding the nozzle. The frequency of the standing wave is, in general, given by

$$f_s = am/2x, \tag{4}$$

where m is an integer. The highest-magnitude acoustic resonance will occur when the phase-lock condition, expressed by (3), and the standing wave condition, expressed by (4), are satisfied simultaneously. Equating f_v from (3) with f_s, and taking $M_j = 0.9$, and $m = 2$ for the present case (from the experimental data), both conditions are met approximately when $n = 3$.

In addition to the match between the vortex-shedding frequency, which is linked to the phase-lock mechanism, and the standing-wave frequency, the measured pure tone frequency of 2300 Hz also corresponds roughly to the aforementioned primary longitudinal mode of the upstream settling tank. This triple-resonance results in a high-magnitude acoustic peak which greatly enhances the T_t separation in the impinging jet. This case serves as a counterpart of the externally excited free jet (§4.1).

Although pure tones are measured at other conditions, and the plot of their frequency versus x/d displays the expected sawtooth pattern characteristic of the lock-on phenomenon, these tones have a much lower magnitude than that of the present case ($x/d = 3$, $M_j = 0.9$), in which the triple-resonance occurs.

To confirm directly the influence of this strong acoustic resonance on the radial profile of $\langle T_w \rangle$, sound-absorbing foam was placed over the wall surrounding the nozzle and data were taken over the entire range of x/d; M_j was held at 0.9. Figure 15 plots the radial profile of $\langle T_w \rangle$ for the acoustically treated nozzle along with the

corresponding frequency spectrum; for convenience the $\langle T_w \rangle$ profile measured with the bare nozzle is plotted beside it. A comparison between these results, for the acoustically treated nozzle, and those shown in figure 14 (bare metal nozzle) demonstrates that suppressing the acoustic resonance eliminates the anomalous behaviour at $x/d = 3$. The presence of heating in the near field at the resonant condition, which disappeared with suppression of the resonance, suggests strongly that it is due to particles of class B; the entrainment of these particles, which previously showed its effect only in the far field, appears to be greatly accentuated in the near field by acoustic resonance. No significant change in the results for other x/d spacings was observed (figure 16), verifying that acoustic resonance is the key to the behaviour of $\langle T_w \rangle$ at $x/d = 3$. (Even at off-resonant points ($x/d \neq 3$), some discrepancies are observable between the bare nozzle and the foam-covered nozzle. Although the cause of this difference has not been pursued in detail, it appears to be related to the change in surface condition from metal to foam.)

5. Concluding remarks

Pursuing the general theme of total-temperature separation in vortical flows and applying it to jet flows in particular, we have shown that even the weak vortical structures naturally present around a jet can separate the total temperature. By extending this argument to the case of the impinging jet, we were further able to show that the wall temperature distribution is determined by the competing influence of the primary and secondary vortex rings on the global total-temperature distribution. Thus the impinging jet is another example of a problem in which, only through an explicit recognition of the role played by the total temperature, can one adequately interpret the surface temperature of a body immersed in a vortical flow.

The effect of viscosity is unimportant in the problem of vortex-induced total-temperature separation because in a free jet the bulk of fluid particles experiencing T_t separation are those entrained originally from the uncontaminated surrounding fluid; the particles initially in the nozzle boundary layer are confined to a very small area in the jet, and thus do not exert a global influence. Even near an impingement surface, the effect of entrainment is essentially to preserve the inviscid process.

The region of cooling induced by the secondary vortex rings when the thermally insulated impingement plate is close to the jet exit would correspond to a region of high heat transfer rate if the plate were heated and thermally conducting; thus the twin peaks of the heat transfer data obtained by Goldstein *et al.* (1986) may be explainable in terms of the model presented here. The seemingly anomalous behaviour of $\langle T_w \rangle$, which is found to be caused by acoustic resonance, may also explain what was previously considered to be spurious heat transfer data obtained by Gardon & Akfirat (1966), who reported that the phenomenon was accompanied by a loud tonal noise.

In addition to the jet flows studied here and the previously investigated wake flows, the role of vortices in separating the total temperature appears to account for the enhanced heat transfer in other vortex-dominated flows. For instance, the results obtained for the blunt leading edge (Gutmark, Yassour & Wofshtein 1982; Parker & Welsh 1983; Hourigan, Welsh & Welch 1985; Cooper, Sheridan & Flood 1986; Welsh *et al.* 1990; and Hourigan *et al.* 1991) may very well fall into this category.

The authors wish to express their appreciation to Mr R. A. Blair for his help in conducting the experiments and to the referees for their constructive suggestions. This work is supported by AFOSR contract number F49620-88-0041.

Appendix

In the equations for compressible boundary layers, we first combine the x-momentum equation with the energy equation, by multiplying the former by u and adding it to the latter. This yields, for $Pr = 1$,

$$\rho\left[\frac{\partial}{\partial t}(c_p T_t)+u\frac{\partial}{\partial x}(c_p T_t)+v\frac{\partial}{\partial y}(c_p T_t)\right]-\rho v\left[\frac{\partial v}{\partial t}+u\frac{\partial v}{\partial x}+v\frac{\partial v}{\partial y}\right]$$
$$=\frac{\partial p}{\partial t}+\frac{\partial}{\partial y}\left(\mu\frac{\partial}{\partial y}(c_p T_t)\right)-\frac{\partial}{\partial y}\left(\mu v\frac{\partial v}{\partial y}\right), \quad \text{(A 1)}$$

where
$$c_p T_t = c_p T+\tfrac{1}{2}(u^2+v^2), \quad \text{(A 2)}$$

and all other notation is standard.

Next consider a single vortex whose centre is located outside of the boundary layer and moving with a constant speed u_v near a wall. The instantaneous position of the vortex centre is (x_0, y_0). This is sketched in figure 17.

The base flow, in which the vortex is immersed, is taken to be a parallel flow: $u = U(y)$, $v = 0$, $T = T(y)$, where outside the boundary layer, $u = U_\infty$, $T = T_\infty$.

A.1. *Outside the boundary layer*

$$u = U_\infty+\frac{\Gamma}{2\pi}\left(\frac{y-y_0}{r^2}-\frac{y+y_0}{r'^2}\right), \quad \text{(A 3}a\text{)}$$

$$v = \frac{\Gamma}{2\pi}\left(-\frac{1}{r^2}+\frac{1}{r'^2}\right)(x-x_0), \quad \text{(A 3}b\text{)}$$

$$u_v = U_\infty-\Gamma/4\pi y_0, \quad \text{(A 3}c\text{)}$$

where
$$r^2 = (x-x_0)^2+(y-y_0)^2, \quad r'^2 = (x-x_0)^2+(y+y_0)^2.$$

The symmetry of u and asymmetry of v around $x = x_0$ lead to

$$\left.\frac{\partial u}{\partial x}\right|_{x=x_0} = 0, \quad v|_{x=x_0} = 0. \quad \text{(A 4)}$$

If we assume the symmetry of T around $x = x_0$,

$$\left.\frac{\partial T}{\partial x}\right|_{x=x_0} = 0, \quad \text{(A 5)}$$

then, it follows from (A 2), (A 4), and (A 5)

$$\left.\frac{\partial T_t}{\partial x}\right|_{x=x_0} = 0. \quad \text{(A 6)}$$

Thus when one evaluates the inviscid form of (A 1) at $x = x_0$ and makes use of (A 4) and (A 6), one obtains

$$\rho\frac{\partial}{\partial t}(c_p T_t) = \frac{\partial p}{\partial t}. \quad \text{(A 7)}$$

In the usual context of the matched asymptotic expansion, denote by a double suffix the inner limit (i) of the outer inviscid solution (i) at $x = x_0$:

$$T_{t_{ii}} = T_{t_i}(x = x_0, y = 0; t), \text{ etc.} \quad \text{(A 8)}$$

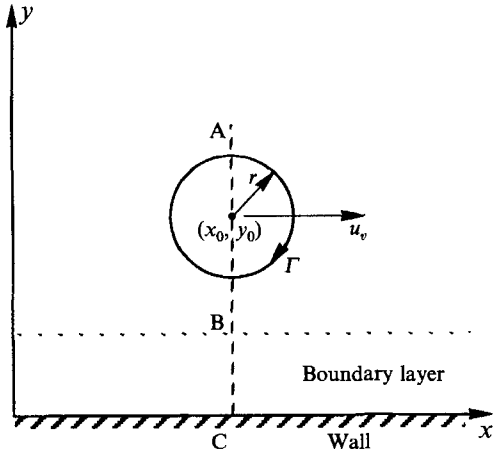

FIGURE 17. Sketch of the vortex moving along a wall.

Then the inviscid equation becomes

$$\rho_{ii}\frac{\partial}{\partial t}(c_p T_{t_{ii}}) = \frac{\partial p_{ii}}{\partial t}. \tag{A 9}$$

A.2. *Inside the boundary layer*

Even within the boundary layer, we assume the symmetry of u and T and asymmetry of v around $x = x_0$; then (A 6) remains valid in the boundary layer. When (A 1) is evaluated at $x = x_0$, it becomes

$$\rho\frac{\partial}{\partial t}(c_p T_t) = \frac{\partial p}{\partial t} + \frac{\partial}{\partial y}\left(\mu\frac{\partial}{\partial y}(c_p T_t)\right), \tag{A 10}$$

which can be written

$$\rho\frac{\partial}{\partial t}(c_p T_t) = \rho_{ii}\frac{\partial}{\partial t}(c_p T_{t_{ii}}) + \frac{\partial}{\partial y}\left(\mu\frac{\partial}{\partial y}(c_p T_t)\right), \tag{A 11}$$

owing to the invariance of pressure across the boundary layer.

For a thermally insulated wall, the boundary condition of $\partial T/\partial y|_{y=0} = 0$ can be rewritten in terms of T_t as

$$\left.\frac{\partial T_t}{\partial y}\right|_{y=0} = 0, \tag{A 12}$$

owing to the non-slip condition.

When the density variation across the boundary layer is negligible

$$T_t = T_{t_{ii}}, \tag{13}$$

which is independent of y, satisfies both (A 11) and (A 12). Therefore for flows with $Pr = 1$, T_t within the boundary layer does not change along the vertical line B–C shown in figure 17 (although T_t outside the boundary layer does change along A–B).

REFERENCES

AHUJA, K. K., LEPICOVSKY, T. & BURRIN, R. H. 1982 *AIAA J.* **20**, 1700–1706.

BADRI-NARAYAN, M. A. & PLATZER, M. F. 1987 In *Turbulence Management and Relaminarisation. IUTAM Symp. Bangalore, India* (ed. H. W. Liepmann & R. Narashima), pp. 471–484. Springer.

BROWN, G. L. & ROSHKO, A. 1974 *J. Fluid Mech.* **48**, 775–816.

COOPER, P. I., SHERIDAN, J. C. & FLOOD, G. J. 1986 *Intl J. Heat Fluid Flow* **7**, 61–68.

CROW, S. C. & CHAMPAGNE, F. H. 1971 *J. Fluid Mech.* **48**, 547–591.

CUMPSTY, N. A. 1978 In *The Aerothermodynamics of Aircraft Gas Turbine Engines*, chap. 24, p. 24-19. AFAPL-TR-78-52.

DIDDEN, N. & HO, C. M. 1985 *J. Fluid Mech.* **160**, 235–256.

DIMOTAKIS, P. E. & BROWN, G. L. 1976 *J. Fluid Mech.* **78**, 535–560.

DIMOTAKIS, P. E., MIAKE-LYE, R. C. & PAPANTONIOU, D. A. 1983 *Phys. Fluids* **26**, 3185–3192.

ECKERT, E. R. G. 1984 *Mech. Engng, N.Y.* **106**, 58–65.

ECKERT, E. R. G. 1986 *Intl Commun. Heat Mass Transfer* **13**, 127–143.

ECKERT, E. R. G. 1987 *Wärme Stoff.* **21**, 73–81.

GARDON, R. & AKFIRAT, J. C. 1966 *Trans. ASME* C: *J. Heat Transfer* **88**, 101–108.

GLASSMAN, I. & JOHN, J. E. A. 1959 *J. Aero/Space Sci.* **26** (6), 387–388.

GOLDSTEIN, R. J., BEHBAHANI, A. I. & HEPPELMANN, K. K. 1986 *Intl J. Heat Mass Transfer* **29**, 1227–1235.

GUTMARK, E., YASSOUR, Y. & WOLFSHTEIN, M. 1982 In *Heat Transfer – 1982 Proc. Seventh Intl Heat Transfer Conf. Munchen, Germany*, pp. 441–445. Hemisphere.

HARTEN, A. & YEE, H. C. 1985 *AIAA* 85–1513.

HEDGES, L. S. 1991 Numerical simulations of acoustic instabilities in the spatially developing, confined supersonic shear layer. PhD thesis, Department of Aeronautics and Astronautics, University of Washington.

HEDGES, L. S. & EBERHARDT, S. E. 1992 *AIAA* 92-0535.

HO, C. M. & NOSSIER, N. S. 1981 *J. Fluid Mech.* **105**, 119–142.

HOURIGAN, K., WELCH, L. W., THOMPSON, M. C., COOPER, P. I. & WELSH, M. C. 1991 *Exp. thermal Fluids Sci.* **4**, 182–191.

HOURIGAN, K., WELSH, M. C. & WELCH, L. W. 1985 In *Advances in Enhanced Heat Transfer – 1985, 23rd Natl Heat Transfer Conf., Denver, CO*, pp. 91–99. ASME.

JALAMANI, Z. A., VAN DALSEM, W. R. & NAKAMURA, S. 1990 *AIAA Paper* 90-1657.

KUROSAKA, M., GERTZ, J. B., GRAHAM, J. E., GOODMAN, J. R., SUNDARAM, P., RINER, W. C., KURODA, H. & HANKEY, W. L. 1987 *J. Fluid Mech.* **178**, 1–29.

LAU, J. C. & FISHER, M. J. 1975 *J. Fluid Mech.* **67**, 229–357.

LEPICOVSKY, J., AHUJA, K. K., BROWN, W. H. & BURRIN, R. H. 1986 *AIAA Paper* 86-1941.

MAGARVEY, R. H. & MACLATCHY, C. S. 1964 *Can. J. Phys.* **42**, 678–683.

NG, W. F., CHAKROUN, W. M. & KUROSAKA, M. 1990 *Phys. Fluids* A **2**, 971–978.

O'CALLAGHAN, J. J. & KUROSAKA, M. 1992 *AIAA Paper* 92-019; also in *AIAA J.* **31**, 1157–1159.

PARKER, R. & WELSH, M. C. 1983 *Intl J. Heat Fluid Flow* **4**, 113–127.

POPIEL, C. O. & TRASS, O. 1991 *Exp. Thermal Fluid Sci.* **4**, 253–264.

PRONCHICK, S. W. & KLINE, S. J. 1983 *Rep.* MD-42. Thermosciences Division, Department of Mechanical Engineering, Stanford University.

SCHNEIDER, P. E. M. 1980 *Z. Flugwiss. Weltraumforsch.* **4**, 307–318.

TSO, J., KOVASZNAY, L. S. G. & HUSSAIN, A. K. M. F. 1981 *Trans. ASME* I: *J. Fluids Engng* **103**, 503–508.

WAGNER, F. R. 1971 *Z. Flugwiss.* **19**, 30–44.

WALKER, J. D. A., SMITH, C. R., CERRA, A. W. & DOLIGALSKI, T. L. 1987 *J. Fluid Mech.* **181**, 99–140.

WELSH, M. C., HOURIGAN, K., DOWNIE, R. J., THOMPSON, M. C. & STOKES, A. N. 1990 *Exp. Thermal Fluid Sci.* **3**, 138–152.

YAMADA, H. & MATSUI, T. 1980 In *Proc. 2nd Intl Symp. on Flow Visualization, Bochum, West Germany*, pp. 355–359. Hemisphere.

YULE, A. J. 1978 *J. Fluid Mech.* **89**, 413–432.

ZAMAN, K. B. M. Q. & HUSSAIN, A. K. M. F. 1980 *J. Fluid Mech.* **101**, 449–491.